Draft version August 31, 2022
Typeset using LaTeX **twocolumn** style in AASTeX631

Star Formation in The Antennae Overlap

Grace Krahm[1] and Molly K. Finn[2]

[1]*Department of Physics and Astronomy, Agnes Scott College, Decatur, GA 30030, USA*
[2]*Department of Astronomy, University of Virginia, Charlottesville, VA 22904, USA*

ABSTRACT

We present ~ 0.1" resolution (~ 10 pc) observations of ^{12}CO$(2-1)$,^{13} CO$(2-1)$, and ^{12}CO$(3-2)$ of the merging Antennae galaxies (NGC 4038 and NGC 4039) taken with the Atacama Large Millimeter/Submillimeter Array (ALMA). We decomposed the emission into individual molecular clouds and calculated their physical properties including their sizes, masses, densities, pressures, and virial parameters. These properties were compared to those of molecular clouds in other galaxies showing that the clouds in the Antennae overlap have similar properties to those in other starbursting galaxies that are capable of forming super star clusters. The molecular clouds in starbursting regions have significantly different properties than those in non-starbursting galactic disks. However, they are not significantly different than molecular clouds in the galactic center of non-starbursting galaxies.

1. INTRODUCTION

Due to their old ages and abundance throughout the observed universe, globular clusters have been used as probes to study stellar and galactic formation in the early universe (Finn et al. 2019). In order to better understand how globular clusters formed, we must look at young star clusters and the molecular gas surrounding them.

Super star clusters (SSCs) are young star clusters that are extremely dense, with average ranges of radii and masses being 1-5 pc (Larsen 2010; Wei et al. 2012) and $10^4 - 10^6 M_\odot$ (Wei et al. 2012) respectively. Due to SSCs having similar sizes and masses to globular clusters, it is believed that SSCs are early-stage globular clusters (McCrady & Graham 2007). This grants more evidence to the idea that the processes that formed globular clusters are still occurring, although only in extreme environments, rather than being confined to the early universe (Ashman & Zepf 2001; McLaughlin & Fall 2008; O'Connell et al. 1994).

In order to form a SSC, and by extension a globular cluster, the progenitor giant molecular cloud (GMC) would need a radius of < 25 pc and a mass $> 10^6$ (Johnson et al. 2015), and an external pressure of $P/k > 10^7$ K cm^{-3} (Elmegreen & Efremov 1997). This is calculated by assuming the typical globular cluster has a half-light radius of 10 pc (van den Bergh et al. 1991), stellar mass of $10^5 M_\odot$ (Harris & Pudritz 1994), and a star formation efficiency (SFE) of $20 - 50\%$ (Ashman & Zepf 2001). These conditions are typically found in galaxy mergers or close interactions which cause the galaxies to starburst which refers to a period of intense star formation.

At a distance of 22 Mpc (Schweizer et al. 2008), the merging Antennae galaxies are the closest major galaxy merger. The overlap region of the Antennae has shown to have the required high density and pressure to form SSCs with the discovery of multiple SSCs (Tsuge et al. 2021; Gilbert & Graham 2007) and a pre-SSC cloud called the Firecracker (Finn et al. 2019; Whitmore et al. 2014).

In this paper we present high-resolution ALMA observations of 12 to characterize the physical conditions of GMCs in the Antennae overlap region and how they compare to GMCs in other galaxies (both SSC-forming and non SSC-forming). In Section 2 we discuss the observations of the Antennae overlap used in this analysis. Section 3 describes the different methods we used for identifying individual GMCs and characterizing the overall structure of the overlap region which we then calculate the physical properties of in Section 4. We then compare those calculated physical properties to those of GMCs in

2. OBSERVATIONS

We used ALMA data from projects 2015.1.00977.S and 2016.1.00924.S during Cycles 3 and 4. This includes both Band 6 and 7 observations of the Antennae overlap region what is summarized in Table 1. After bandpass and phase calibration, the observations were then reduced and calibrated using the CASA 4.7.2 pipeline. A more in-depth description of the observation parameters and calibration is available in Finn et al. (2019).

3. STRUCTURE DECOMPOSITION

We used two different methods to decompose the structure of the Antennae overlap region called clumps and dendrograms. For all counting-based analysis we split the emission into singular clumps that do not overlap with one another. However, clump-finding algorithms do not capture the hierarchical nature of molecular clouds and are biased towards finding circular, beam-

Table 1: Antennae Overlap Observations

Line	Beam (")	RMS (K)	Channel Width (km/s)
^{12}CO$(2-1)$	0.180 x 0.166	0.846	5
^{12}CO$(3-2)$	0.180 x 0.166	0.629	5
^{13}CO$(2-1)$	0.180 x 0.166	0.242	5

sized clouds. Dendrogram algorithms eliminate these issues by splitting the emission into a hierarchy of structures, although they can only be used for non counting-based analysis since areas of emission are counted multiple times.

3.1. *Clumps*

We used the `quickclump` (Sidorin 2017) algorithm to divide the emission into clumps. Because the calibration artificially brightened some areas, the algorithm identified certain pockets of noise as emission. In order to exclude as much noise as possible without losing areas of emission, we ran the algorithm with two different sets of parameters, broad and narrow. The broad parameters consisted of `Nlevels`=1000, `Tcutoff`= 5σ, `dTleaf`= 5σ, and `Npixmin`=350 ($\sim$ 2 beams), while the narrow parameters consisted of `Nlevels`=1000, `Tcutoff`= 11σ, `dTleaf`= 11σ, and `Npixmin`=180 ($\sim$ 1 beam). The clumps found with the broad parameters were used for the majority of the analysis, with the narrow parameter clumps being used for additional clump mass and radius calculations.

3.2. *Dendrogram Structures*

We used the package `astrodendro` (Rosolowsky et al. 2008) to decompose the emission into hierarchical structures which are separated into three categories: leaves, branches, and trunks. Leaves are the most isolated category which represent clouds with no resolved substructure. Branches are larger structures than leaves which both have substructures as well as being smaller substructures of larger cloud structures called trunks. Trunks are the largest structures and are not substructures of any other cloud. Isolated clouds that neither have substructure nor are part of larger structures can be categorized as both trunks and leaves, however they are sorted into the leaf category by convention. The structures identified in the Antennae overlap region were found using the following parameters: `min_value`= 5σ, `min_delta`= 2.5σ, and `min_npix`=2 beams. These structures are visualized in the dendrogram in Figure 1 and are treated as individual GMCs for the rest of the analysis.

3.2.1. *Fractal Dimension*

One of the ways to quantify the morphology of molecular cloud structures is by calculating the region's fractal dimension, D_2. This is calculated by fitting the area-perimeter relation $P \propto A^{\frac{1}{2}D_2}$ (Falgarone et al. 1991) to the dendrogram structures (`scipy.optimize.curve_fit` Virtanen et al. (2020)).

Figure 2 shows the ^{12}CO(2-1) and ^{12}CO(3-2) emissions having very similar morphology while the ^{13}CO(2-1) emission has slightly higher morphology. All three are above the $D_2 = 1.36 \pm 0.02$ measured for ^{12}CO (using ^{12}CO$(1-0)$, ^{12}CO$(2-1)$, and ^{12}CO$(3-2)$) for galactic GMCs (Falgarone et al. 1991). However, both the ^{12}CO$(2-1)$ and ^{12}CO$(3-2)$ emissions are within the range 1.2-1.5 range for HI emission in galactic GMCs (Sánchez et al. 2007) with the ^{13}CO$(2-1)$ emission being slightly higher at $D_2 = 1.517$. This suggests that, while the turbulent structure of GMCs in the Antennae overlap tends to be on the higher end of fractal dimensions calculated for galactic GMCs, they are still fairly comparable.

4. CALCULATING PHYSICAL PROPERTIES

We calculated the radius, linewidth, mass, virial parameter α_{vir}, and for each molecular cloud identified by the `quickclump` and `astrodendro` algorithms. The properties calculated in this section are summarized in Tables A1 - A6 and are used in the analysis in Section 5.

4.1. *Sizes and Linewidths*

The radius of each clump was found by fitting an ellipse to the half-width at half-max (HWHM) of the clump. The fitted major and minor axis of the ellipse was then converted into the radius of a circle with the same area

$$R = \sqrt{\sigma_{maj}\sigma_{min}}. \quad (1)$$

The error in R, σ_R, was then estimated based on the circularity of the fitted ellipse. The velocity dispersion and its error, σ_v and σ_{σ_v}, were found by fitting Gaussians (`scipy.optimize.curve_fit` Virtanen et al. (2020)) to the intensity-weighted mean line profiles. From the fitted Gaussian, σ_v was taken from the equivalent width and σ_{σ_v} from the corresponding value in covariance matrix. R and σ_v were then deconvolved by using Equations (2) and (3) respectively.

$$R_{deconvolved} = \sqrt{R^2 - (\theta_{beam}/2)^2}, \quad (2)$$

$$\sigma_{v,deconvolved} = \sqrt{\sigma_v^2 - (\delta_v/2.35)^2}, \quad (3)$$

Here θ_{beam} is the beam size in pc, and δ_v is the velocity resolution of 5 km/s. R was additionally scaled by 1.91 to convert $R_{deconvolved}$ into an effective radius (Solomon et al. 1987). For the rest of this paper, σ_v and R refer to the deconvolved velocity dispersions and effective radii.

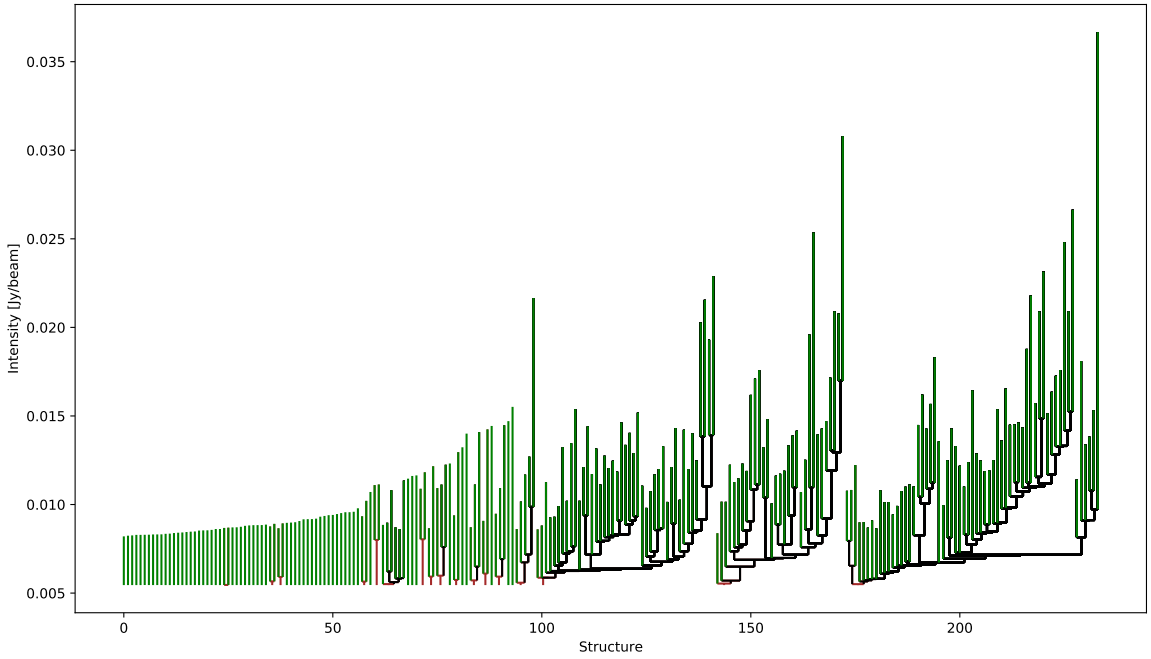

Figure 1: Dendrogram for the overlap region created by `astrodendro` where vertical line is a structure. The red lines are trunks, black lines are branches, and green lines are leaves.

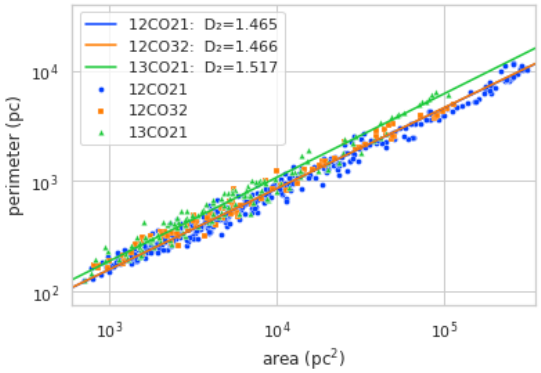

Figure 2: Perimeter of the dendrogram structures for ^{12}CO(2-1), ^{12}CO(3-2), and ^{13}CO(2-1) plotted against their full-width at half-max (FWHM) areas.

4.2. *Mass*

The cloud masses were calculated using the $^{12}\mathrm{CO}(2-1)$ and $^{13}\mathrm{CO}(2-1)$ lines which we assumed to be optically thick and optically thin respectively. We also assumed that the clouds are in local thermodynamic equilibrium (LTE) and that the excitation temperature, T_x, is the same for all velocities within a cloud. Using these assumptions, the general equation,

$$T_b = (1 - e^{-\tau_\nu}) \left[\frac{1}{e^{\frac{T_{ul}}{T_x}} - 1} - \frac{1}{e^{\frac{T_{ul}}{T_{bg}}} - 1} \right], \tag{4}$$

can be rearranged and simplified to

$$T_{x,12} = T_{ul} \left[ln \left(\frac{-T_{12} e^{\frac{T_{ul,12}}{T_{bg}}} + T_{12} - T_{ul} e^{\frac{T_{ul}}{T_{bg}}}}{T_{ul,12} - T_{12} e^{\frac{T_{ul,12}}{T_{bg}}} + T_{12}} \right) \right]^{-1} \tag{5}$$

where T_{12} is the brightness temperature for $^{12}\mathrm{CO}(2-1)$, $T_{ul,12} = 11.07$ K and $T_{bg} = 2.73$ K. Assuming that $T_{x,12} = T_{x,13} = T_x$, T can then be plugged back in to Equation (4) for $^{13}\mathrm{CO}(2-1)$. Because $^{13}\mathrm{CO}(2-1)$ is optically thin, the optical depth term, $(1 - e^{-\tau_\nu})$, is left in and the equation can be rearranged to calculate $\tau_{\nu,13}$ at each pixel in the cloud

$$\tau_{\nu,13} = -ln \left[1 - \frac{T_{13}}{T_{ul,13}} \left[\frac{1}{e^{\frac{T_{ul,13}}{T_x}} - 1} - \frac{1}{e^{\frac{T_{ul,13}}{T_{bg}}} - 1} \right] \right]. \tag{6}$$

In Equation (6) above, $T_{ul,13} = 10.58$ K.

We then found the column density at each pixel using the Mangum & Shirley (2015) equation,

$$N_{tot} = \frac{8\pi\nu_0^2 Q}{c^2 A_{ul} g_u} \frac{1}{1 - e^{\frac{-T_{ul,13}}{T_x}}} \int \tau_\nu d\nu. \tag{7}$$

After plugging in $Q = \frac{T_x}{B_0} + \frac{1}{3}$, $B_0 = 2.664$ K, and $\tau_{\nu,13}$, Equation (7) becomes

$$\frac{N_{tot}^{13}}{cm^{-2}} = \frac{8\pi\nu_0^2}{c^2 A_{ul} g_u} \left(\frac{T_x}{2.644} + \frac{1}{3} \right) \frac{1}{1 - e^{\frac{-T_{ul,13}}{T_x}}} \int \tau_{\nu,13} d\nu. \tag{8}$$

. Using Equations (5), (6), and (8), we determined the number column density of ^{13}CO(2-1) per pixel for each clump which we then obtained the mass by summing over all pixels in a clump and multiplying by the area of a pixel (in cm^{-2}). From this we found the H_2 mass by adopting the ratios $\chi_{12}/\chi_{13} \simeq 70$ (Bigiel et al. 2015), $^{12}\mathrm{CO}(2-1)/^{12}\mathrm{CO}(1-0) \simeq 0.5$ (Bigiel et al. 2015), and $H_2/^{12}\mathrm{CO} = 2 \times 10^4$ (Blake et al. 1987; Finn et al. 2019). To obtain the total molecular mass we then multiplied the H_2 mass by a factor of 1.3 (Finn et al. 2019, 2021). We then adopted an error of 10% due to flux uncertainty which was much larger than the error due to σ_{rms} (Finn et al. 2019).

4.3. *Virial Parameter and Cloud Pressure*

Using the R, σ_v, and mass calculated as shown above, we calculated each cloud's virial parameter, α_{vir}. The virial parameter is used to quantify how the gravity of the clouds are balanced with the outward pressure from kinetic energy. α_{vir} is defined as

$$\alpha_{vir} = \frac{5\sigma_v^2 R}{GM} \tag{9}$$

with $\alpha_{vir} = 1$ indicating virial equilibrium. To calculate the external pressure, P_e, that each cloud is subject to using the equation from Elmegreen (1989)

$$P_e = \frac{3\prod M\sigma_v^2}{4\pi R^3} \tag{10}$$

where $\prod = 0.5$ (Johnson et al. 2015).

5. COMPARATIVE ANALYSIS

We compared the calculated properties for our clouds with those of molecular clouds in a selected group of galaxies which are summarized in Table 2. These data sets were chosen due to their similar spatial resolutions and line tracers to our Antennae data. The data sets chosen are separated into four separate groups for analysis: A, B, C, and D. The A group consists of GMCs from areas with a normal amount of star formation and serve as a baseline to compare the other data sets to. Groups B and C are comprised of various types of starbursting galaxies. Group B represents the dwarf starbursts while group C is for the intermediate to large starbursting galaxies. Group D consists of GMCs, in both starbursting and non-starbursting galaxies, that are located in the center of their host galaxies. The starbursting galactic centers are part of both the C and D groups.

5.1. *Size-Linewidth Relations*

The relationship between a cloud's effective radius and linewidth is expected to follow a power law relationship of the form

$$\sigma_v = a_0 R^{a_1} \tag{11}$$

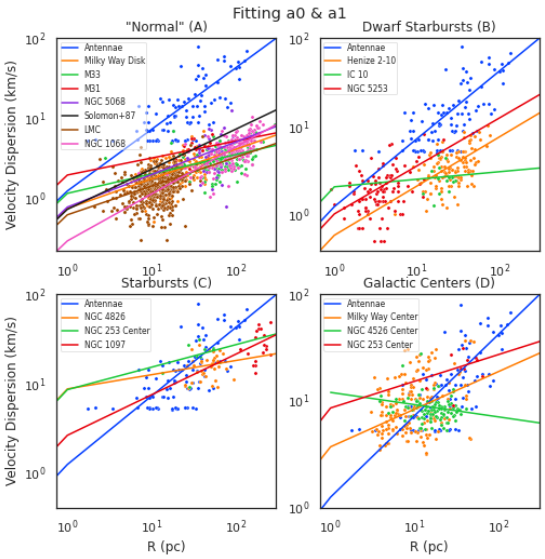

Figure 3: Size-linewidth plots comparing $^{12}\mathrm{CO}(2-1)$ Antennae emission to galaxies in each group A, B, C, and D allowing both parameters in Equation (11) to be fit.

(Larson 1981; Solomon et al. 1987). Using Equation (11), we fit lines to each of our emissions as well as the emissions for the clouds in Table 2. These are plotted in Figure 3 by group with our $^{12}\mathrm{CO}(2-1)$ line in each plot representing the Antennae for comparison. As seen in Figure 3, fitting both the a0 and a1 parameters at once do not easily lend itself to comparison. This is due to the fact that many data sets do not have the necessary range of size scales to robustly fit both parameters. In order to account for this, fit each parameter individually while holding the other at the standard galactic values 0.72 and 0.5 for a0 and a1 respectively (Solomon et al. 1987). The fitted parameter values for each method are summarized in Table 3.

Figure 4 shows the GMCs for the Antennae overlap having very high velocity dispersions for their sizes with their fitted lines having much larger slopes and intercepts than those for any singular group. While the major starbursts (C) and galactic centers (D) come closer than "normal" (A) GMCs or even those from dwarf starbursts (B), the GMCs that have the same level of elevated linewidths as the Antennae overlap are those from NGC 253 which is in both groups C and D. This could suggest that the galactic centers of starbursting galaxies have the most similar conditions to the Antennae overlap, however because we only have one data set that meets the criteria, it is possible that the similarity comes from properties specific to NGC 253 instead.

5.2. *Mass-Based Properties*

When comparing mass-based properties of the Antennae overlap, we limited the comparison galaxies to data

Table 2: Data Sets Used in This Analysis

Galaxy	CO Lines	Distance	Resolution	Channel	Galaxy	Region	Group	Reference
			pc	km/s				
Milky Way	1-0	8.5 kpc	1.4	2	Spiral	Galactic Center	D	1,2
Milky Way	1-0	1.5-13.8 kpc	0.5,3	0.21,1	Spiral	Galactic Disk	A	3
M31	1-0	770 kpc	50,25	1.3	Barred Spiral	Spiral Arm	A	4
M33	1-0	840 kpc	50	1.3	Spiral	Central 5.5 kpc	A	5
Henize 2-10	1-0	8.7 Mpc	26	0.637	BCD Starburst		B	6
NGC 5068	2-1	5.2 Mpc	26	2.5	Barred Spiral		A	7
NGC 4826	2-1	2.2 Mpc	27	2.5	Spiral Starburst		C	7
NGC 4526	2-1	16.4 Mpc	20	10	Lenticular	Galactic Center	D	8
IC 10	1-0	950 kpc	20	1,3,4	Dwarf Starburst	Disk & Envelope	B	9
NGC 253	1-0	3.5 Mpc	35	5	Spiral Starburst	Galactic Center	C,D	10
NGC 5253	2-1	3.15 Mpc	3	1.47	BCD Starburst		B	11
LMC	1-0	50 kpc	11	0.5	Dwarf		A	12
NGC 1068	^{13}CO(1-0)	14.4 Mpc	100	19	Spiral		A	13
NGC 1097	2-1	14.5 Mpc	100	30	Barred Spiral	Starbursting Ring	C	14

NOTE—All emission lines are ^{12}CO except for the Milky Way disk data which uses the ^{13}CO(2-1) line

.

References—(1) Oka et al. (2001); (2) Miyazaki & Tsuboi (2000); (3) Heyer et al. (2008); (4) Rosolowsky (2007); (5) Rosolowsky et al. (2007); (6) Imara & Faesi (2019); (7) Rosolowsky et al. (2021); (8) Utomo et al. (2015); (9) Leroy et al. (2006); (10) Leroy et al. (2015); (11) Miura et al. (2018); (12) Wong et al. (2011); (13) Tosaki et al. (2017); (14) Hsieh et al. (2011)

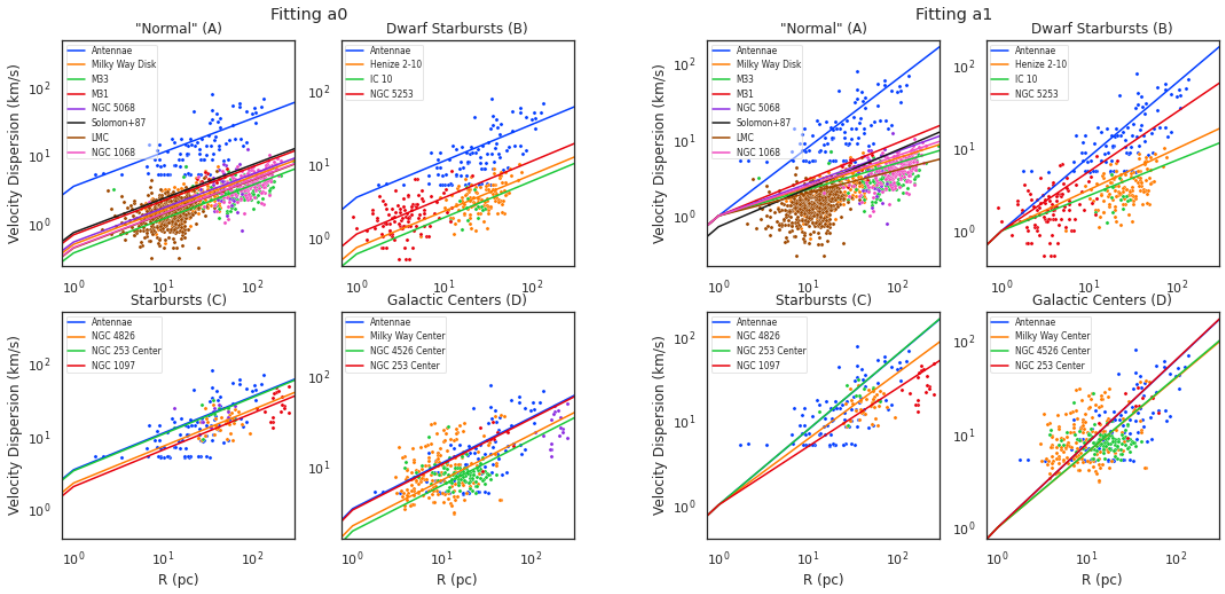

Figure 4: Size-linewidth plots comparing ^{12}CO$(2-1)$ Antennae emission to galaxies in each group A, B, C, and D. The left image shows the plots where a1=0.5 is assumed and the a0 parameter is fitted to each data set while the image on the right shows a0=1 being held constant while a1 is fitted for each data set.

Table 3: Size-Linewidth Line Fit Parameters

Galaxy	Category	Fit a0 and a1		a1=0.5	a0=1
		(a0)	(a1)	(a0)	(a1)
Antennae ^{12}CO(2 − 1)		1.22	0.77	3.47	0.89
Antennae ^{12}CO(3 − 2)		5.12	0.50	5.05	0.92
Antennae ^{13}CO(2 − 1)		1.28	0.70	2.93	0.82
Milky Way	A	3.64	0.36	2.25	0.80
Milky Way	D	0.74	0.37	0.48	0.38
M31	A	1.14	0.24	0.36	0.35
M33	A	1.93	0.21	0.67	0.48
Henize 2-10	B	0.58	0.56	0.71	0.5
NGC 5068	A	0.77	0.41	0.52	0.42
NGC 4826	C	8.61	0.16	2.28	0.78
NGC 4526	D	11.84	0.12	1.97	0.80
IC 10	B	2.05	0.09	0.58	0.43
NGC 253	C,D	8.45	0.35	3.36	0.90
NGC 5253	B	1.01	0.54	1.08	0.72
LMC	A	0.62	0.36	0.43	0.30
NGC 1068	A	0.3	0.59	0.43	0.39
NGC 1097	C	2.6	0.46	2.04	0.69

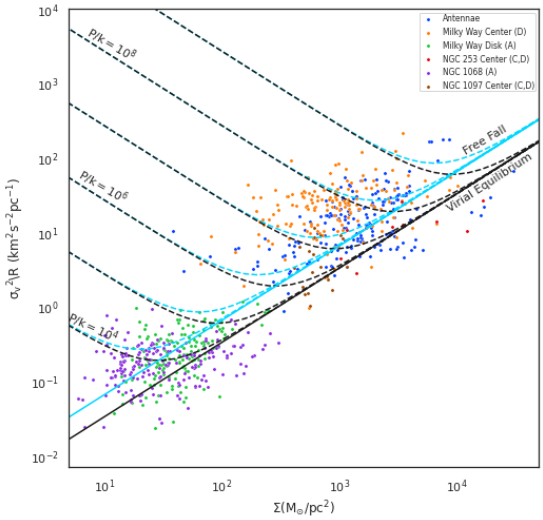

Figure 5: Surface density plotted against the velocity metric σ_v^2/R. The black lines represent virial equilibrium and the cyan lines represent free fall. The dashed black and cyan lines represent those same conditions accounting for external pressure ranging from $10^4 - 10^9$ K cm^{-3}.

sets which calculated mass using the same LTE method that we used. In addition to being more sensitive to cloud conditions varying throughout a galaxy, this also allows us to draw more direct comparisons between each data set. However, because the LTE method is not as common as using an X_{CO} conversion factor, there are fewer GMC data sets to compare to. This includes all of GMCs in the dwarf starburst group (B). For the remaining GMC data sets, we compared their virialization, pressures, and surface densities in Sections 5.2.1 and 5.2.2 respectively.

5.2.1. *Virialization and Pressure*

Figure 5 shows most of the GMC data sets generally falling around the virialization and free-fall lines in black and cyan respectively. The GMCs from the Milky Way disk tend a little higher above the free fall line while GMCs from NGC 253 tend to fall a little more below the virial equilibrium line, however they're still generally clumped around the two lines. The major exceptions are the Milky Way center and the Antennae overlap with their GMCs falling further above the free fall line than any of the others.

These GMCs are also affected by much higher pressures than the other GMCs as shown by the dashed black and cyan lines. Qualitatively, the GMCs from the Milky Way disk and the Antennae overlap seem to have external pressures ranging from $10^6 - 10^9$ K cm^{-3} while GMCs from group A have pressures of at most 10^5 K cm^{-3}.

Both the virialization and external pressures of the clouds are more quantitatively shown in Figures 6 and 7 of the α_{vir} and P_e calculated in Section 5.2.1. The plots

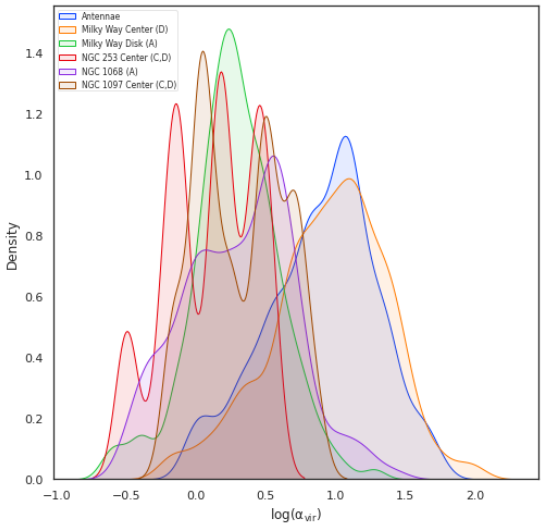

Figure 6: Kernel density estimate of α_{vir} for each of the GMC data sets.

are shown as kernel density with kernel widths of 25% for ease of viewing.

Figure 6 shows even more clearly how most of the GMCs have similar α_{vir} values with the kernel density estimate plots completely overlapping. The exceptions, the Antennae overlap and the Milky Way center, do have some GMCs in the typical range but most of their GMCs have much higher α_{vir} values than the other data sets. This shows that the GMCs of the two exceptions require an external pressure to be bound.

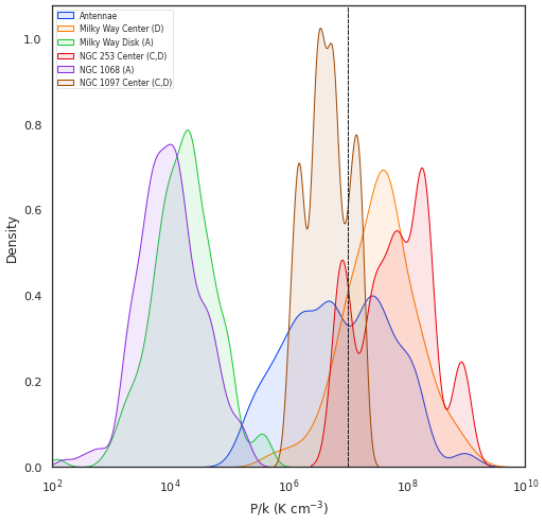

Figure 7: Kernel density estimate of P_e/k for each of the GMC data sets. The dotted black line represents $P/k = 10^7$ K cm^{-3} typically required for SSC formation (Elmegreen & Efremov 1997).

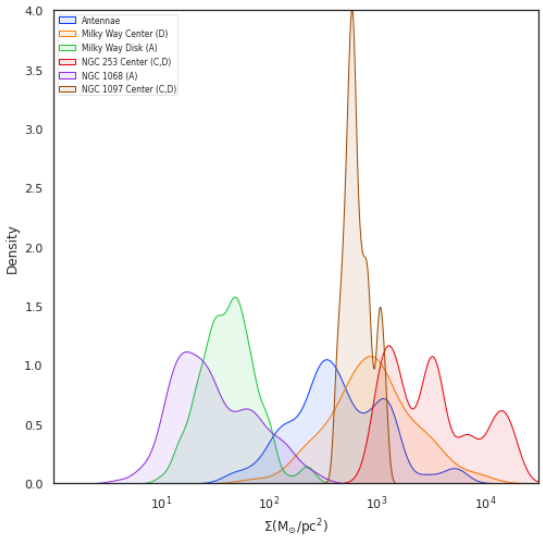

Figure 8: Kernel density estimate of the surface density, $\Sigma(M_\odot/pc^2)$, for each of the GMC data sets.

These high pressures needed to hold together the GMCs of the Antennae overlap and the Milky Way center are shown in Figure 7. Like in Figure 5, the kernel density estimate shows the Antennae overlap and the Milky Way center having higher pressures than GMCs in group A. However, the high pressures of the GMCs in NGC 253 and NGC 1097 are also shown here where they were not as easily seen in Figure 5.

5.2.2. *Surface Density*

Figure 8 shows the kernel density estimate of the surface density, $\log(\Sigma)(M_\odot/pc^2)$, of the GMCs. This shows a similar trend to Figure 7 with the Antennae overlap and other GMCs in groups C and D having higher surface densities than GMCs in group A. With the exception of NGC 1097, the surface densities are more dispersed and are not as clearly separated as the pressures are though the general trend still holds.

6. DISCUSSION

The Antennae overlap and other starbursting galaxies having higher pressures and densities as shown in Section 5.2 consistent with the conditions needed for SSC formation. However, these conditions are not unique to SSC-forming galaxies. The Milky Way center, which is not forming SSCs, also has GMCs with similar high pressures and densities. This indicates that there are other factors that allow for SSC formation in starbursting galaxies that have not yet been identified. Dwarf starbursts are another avenue of interest since many of them are much closer than major mergers, allowing for better resolution data of their GMCs. However, their mass-based properties can not be directly compared to the Antennae overlap due to different mass calculations. All of the data sets in the dwarf starburst group (B), used an X_{CO} conversion factor which is both difficult to characterize for starbursts as well as not allowing for variations in excitation conditions among GMCs within a galaxy. The lower linewidths in Figure 4 do show that dwarf starbursts have different properties than major starbursts despite both being able to form SSCs.

7. CONCLUSION

We present high-resolution ($\sim$ 10 pc) ALMA observations of the overlap region of the Antennae galaxies (NGC 4038/39). The emission from $^{12}CO(2-1)$, $^{12}CO(3-2)$, and $^{13}CO(2-1)$ were use to characterize GMCs and their environments which we then compared to GMCs from other galaxies summarized in Table 2. The primary findings are as follows:

- The $^{12}CO(2-1)$, $^{12}CO(3-2)$, and $^{13}CO(2-1)$ emissions have fractal dimensions of $D_2 = 1.465$, 1.466, and 1.517 respectively. These are in the upper range of measurements, but not significantly different, when compared to fractal dimensions measured in HI emission in galactic clouds. (Section 3.2.1)

- We calculated the velocity dispersion, effective radius, mass, surface density, pressure, and α_{vir} of each GMC in the Antennae overlap region summarized in Tables A1 - A6. (Section 4 and Appendix A)

- Comparing the size-linewidth relations of the Antennae overlap to those for "normal" non starbursting GMCs (group A), dwarf starburst galaxies (B), major starbursting galaxies (C), and galactic centers (D), the Antennae overlap has much

higher turbulent kinetic energy than any singular group. Groups A and B had the lowest kinetic energy while GMCs solely in group C or D showed higher kinetic energy than the other groups, but not as much as the Antennae. NGC 253 which was in both groups C and D had comparable kinetic energy levels to the Antennae overlap region. (Section 5.1)

- The Antennae overlap as well as the Milky Way galactic center have higher $\alpha_{\rm vir}$ values than the other galaxies they were compared to, indicating that would both require an external pressure to be bound. (Section 5.2.1)

- The GMCs in starbursting galaxies or galactic centers, including the Antennae overlap, have higher pressures than GMCs from the non-starbursting NGC 1068 and Milky Way disk (group A). (Section 5.2.1)

- Like with pressure, GMCs in the starbursting galaxies and in galactic centers have higher surface densities than those in group A. However, due to the wide variety of GMCs and low surface densities when compared to other major starbursts, there is still some overlap. Some of the less extreme GMCs in the Antennae overlap have similar properties to the more extreme GMCs in group A. (Section 5.2.2)

- The GMCs in the Antennae overlap as well as other starbursts have kinetic energies, pressures, and surface densities that are significantly higher than those non-starbursting areas. Despite this, the non-SSC-forming Milky Way center also has similar elevated levels of kinetic energy, pressure, and molecular gas density as starbursts. This indicates that there are other factors, likely only visible in sub 10 pc resolution, that allow SSC formation. (Section 6)

Software: Astrodendro (Rosolowsky et al. 2008), Astropy (Astropy Collaboration et al. 2013, 2018), NumPy (Harris et al. 2020), Quickclump (Sidorin 2017), SciPy (Virtanen et al. 2020),

APPENDIX

A. GMC CATALOGS

GMC catalogs for each emission line observed for the Antennae overlap. Each emission has two catalogs: one using clump decomposition and the other using dendrogram decomposition. Unless otherwise stated, the properties are calculated and labeled as described in Section 4.

[h]

Table A1: ^{12}CO$(2-1)$ Clump Properties

ncl	CO max (K)	σ_v (K km/s)	σ_v error (K km/s)	maj x min (pc x pc)	R (pc)	R error (pc)
1	28.44	78.64	3.62	18.74 x 31.10	35.07	11.97
2	23.88	51.28	1.76	36.72 x 58.38	73.17	15.98
3	20.66	50.36	2.18	71.43 x 61.00	105.80	27.77
4	19.66	31.35	1.31	35.73 x 21.97	40.86	10.24
5	19.24	42.89	1.61	69.81 x 64.81	107.90	25.49
6	17.95	41.54	1.66	55.03 x 70.84	99.96	30.15
7	17.75	28.11	1.15	29.81 x 50.43	60.52	19.34
8	16.90	41.54	1.68	31.30 x 22.80	39.70	12.95
9	16.80	17.18	0.81	11.92 x 17.90	15.92	3.67
10	16.72	67.86	3.54	46.10 x 154.70	136.10	71.20

area (10^3pc^2)	perimeter ($(10^3$pc)	virial mass ($(10^7 M_\odot$)	LTE mass ($(10^6 M_\odot$)	Σ ($(10^2_\odot$/pc^2)	P/k (K cm^{-3})	α_{vir}
13.09	0.887	25.21	11.12	28.78	93.48	22.59
21.15	0.9676	22.37	23.06	13.71	9.08	9.66
72.93	2.673	31.19	51.04	14.51	6.41	6.09
8.988	0.7257	4.67	5.97	11.38	5.04	7.79
61.75	2.338	23.07	41.75	11.41	3.58	5.51
35.28	1.705	20.05	17.44	5.56	1.77	11.45
22.95	1.218	5.56	15.61	13.57	3.26	3.55
9.289	0.6899	7.96	7.30	14.75	11.81	10.87
14.22	1.383	0.55	4.42	55.54	18.97	1.23
68.82	2.992	72.86	42.42	7.29	4.54	17.11

NOTE—Table of observed properties of the ^{12}CO(2-1) emission of the Antennae overlap where "ncl" is the cloud number, "CO max" is the maximum brightness in the clump, "σ_v" is the velocity dispersion, "maj x min" are the major and minor axes of the clump, "R" is the clump's effective radius, and Σ is the clump's surface density. The first 10 clumps are shown here with the full table being available upon request.

[h]

Table A2: ^{12}CO(2 − 1) Dendrogram Properties

ncl	clump type	CO max (K)	σ_v (km/s)	σ_v error (km/s)	maj x min (pc)	R (pc)	R error (pc)
0	trunk	23.88	88.29	4.25	243.07 x 104.64	258.64	119.68
1	trunk	23.88	88.16	4.23	242.11 x 104.09	257.45	120.65
2	trunk	23.88	86.08	4.08	242.65 x 104.45	258.19	97.66
3	trunk	23.88	84.32	3.98	104.58 x 245.9	260.07	63.67
4	trunk	23.88	84.18	3.99	180.51 x 82.83	197.98	74.18
5	trunk	23.88	55.47	2.24	115.5 x 90.04	164.83	46.28
6	trunk	23.88	84.34	3.99	100.9 x 259.63	262.51	125.22
7	trunk	23.88	55.53	2.25	114.7 x 87.14	161.56	45.64
8	trunk	23.88	53.62	2.16	29.8 x 103.43	88.52	58.45
9	trunk	23.88	51.84	2.06	29.55 x 102.09	87.53	58.90

area (10^3pc^2)	perimeter (10^3pc)	LTE mass (10^7 M$_\odot$)	Σ (10^2M$_\odot$/pc^2)	P/k (10^7 K cm^{-3})	α_{vir}
191104.85	7364.58	29.58	14.08	7.81	7.89
186351.09	7295.90	28.91	13.88	7.72	8.02
175806.74	6886.75	27.62	13.19	6.97	8.02
141836.96	6373.08	22.60	10.64	5.36	9.47
81293.37	4243.74	15.96	12.96	8.55	10.18
45042.58	2245.81	10.41	12.20	4.20	5.64
84203.15	4079.49	16.76	7.74	3.86	12.90
42164.01	2215.95	9.76	11.91	4.19	5.91
30600.68	1523.09	7.91	32.12	19.22	3.73
26181.37	1230.42	7.32	30.41	17.20	3.72

NOTE—Table of observed properties of the ^{12}CO(2-1) emission of the Antennae overlap where "ncl" is the cloud number, "clump type" is the dendrogram structure type of the cloud, "CO max" is the maximum brightness in the clump, "σ_v" is the velocity dispersion, "maj x min" are the major and minor axes of the clump, "R" is the clump's effective radius, and Σ is the clump's surface density. The first 10 structures are shown here with the full table being available upon request.

Table A3: ^{12}CO(3 − 2) Clump Properties

ncl	CO max	σ_v	σ_v error	maj x min	R	R error	area	perimeter
	(K)	(km/s)	(km/s)	(pc)	(pc)	(pc)	(10^3pc^2)	(10^2pc)
1	27.07	76.16	3.54	17.42 x 28.84	31.89	7.98	12.64	10.66
2	14.82	45.86	2.04	62.73 x 53.6	92.59	23.99	35.92	18.67
3	13.09	40.94	1.80	68.69 x 35.01	77.74	24.69	34.27	16.46
4	12.36	47.70	2.10	19.77 x 45.13	45.25	27.13	18.64	17.02
5	11.57	32.93	1.27	20.18 x 42.43	44.19	18.07	12.08	8.84
6	10.87	39.02	1.68	35.72 x 52.95	68.46	22.65	16.76	11.77
7	10.87	32.70	1.26	19.85 x 27.33	33.51	3.28	4.39	3.91
8	10.50	33.87	1.51	32.49 x 57.52	68.02	22.43	14.29	9.89
9	10.08	15.06	0.59	17.07 x 31.77	33.51	10.85	3.49	4.36
10	9.77	27.81	1.32	20.4 x 22	29.59	4.23	6.86	6.66

NOTE—Table of observed properties of the ^{12}CO(3-2) emission of the Antennae overlap where "ncl" is the cloud number, "CO max" is the maximum brightness in the clump, "σ_v" is the velocity dispersion, "maj x min" are the major and minor axes of the clump, and "R" is the clump's effective radius. The first 10 clumps are shown here with the full table being available upon request.

Table A4: ^{12}CO(3 − 2) Dendrogram Properties

ncl	clump typ	CO max	σ_v	σ_v error	maj x min	R	R error	area	perimeter
		(K)	(km/s)	(km/s)	(pc)	(pc)	(pc)	(10^3pc^2)	(10^2pc)
0	trunk	11.57	44.19	1.88	26.24 x 90.33	77.16	39.72	19.03	14.01
1	leaf	7.20	35.09	1.67	18.55 x 22.66	28.29	8.43	3.92	4.63
2	trunk	8.62	47.79	2.43	51.32 x 13.82	39.55	15.37	7.09	6.21
3	leaf	8.62	22.34	1.03	21.47 x 15.53	23.89	8.20	4.32	4.00
4	trunk	14.82	67.03	2.93	145.98 x 60.15	151.30	45.58	113.05	50.08
5	trunk	14.82	67.05	2.93	149.49 x 62.08	155.61	35.65	102.58	45.21
6	trunk	14.82	65.43	2.89	147.54 x 60.53	152.60	57.50	96.13	43.39
7	trunk	14.82	65.21	2.85	148.63 x 60.22	152.77	57.94	86.86	37.51
8	trunk	14.82	65.23	2.85	147.33 x 59.79	151.55	58.78	88.92	38.67
9	trunk	14.82	65.44	2.89	148.92 x 61.47	154.53	44.56	98.62	43.18
10	trunk	14.82	65.23	2.85	147.02 x 59.71	151.28	61.91	90.21	39.51

NOTE—Table of observed properties of the ^{12}CO(3-2) emission of the Antennae overlap where "ncl" is the cloud number, "clump type" is the dendrogram structure type of the cloud, "CO max" is the maximum brightness in the clump, "σ_v" is the velocity dispersion, "maj x min" are the major and minor axes of the clump, and "R" is the clump's effective radius. The first 10 structures are shown here with the full table being available upon request

Table A5: ^{13}CO(2 – 1) Clump Properties

ncl	CO max	σ_v	σ_v error	maj x min	R	R error	area	perimeter
	(K)	(km/s)	(km/s)	(pc)	(pc)	(pc)	(10^3pc^2)	(10^2pc)
1	6.01	24.90	0.84	16.93 x 35.73	35.90	17.92	13.90	8.78
2	4.87	19.65	0.58	22.75 x 30.2	38.80	9.48	9.50	7.26
3	4.53	33.32	1.47	25 x 66.48	63.89	38.62	14.89	15.14
4	4.41	20.64	0.71	45.11 x 19.14	44.40	15.85	10.70	8.72
5	4.31	26.64	1.06	33.76 x 44.35	60.38	15.23	17.53	15.56
6	4.23	13.14	0.48	18.04 x 33.22	35.68	17.70	5.18	6.90
7	3.77	19.63	0.83	20.11 x 15.8	23.01	7.13	4.59	5.05
8	3.67	24.81	0.98	17.47 x 31.53	33.84	19.65	7.82	6.72
9	3.66	18.83	0.87	17.34 x 29.04	31.95	14.43	5.52	7.20
10	3.42	9.75	0.35	34.99 x 13.27	30.28	21.14	5.00	5.94

NOTE—Table of observed properties of the ^{13}CO(3-2) emission of the Antennae overlap where "ncl" is the cloud number, "CO max" is the maximum brightness in the clump, "σ_v" is the velocity dispersion, "maj x min" are the major and minor axes of the clump, and "R" is the clump's effective radius. The first 10 clumps are shown here with the full table being available upon request.

Table A6: ^{13}CO(2 – 1) Dendrogram Properties

ncl	clump typ	CO max	σ_v	σ_v error	maj x min	R	R error	area	perimeter
		(K)	(km/s)	(km/s)	(pc)	(pc)	(pc)	(10^3pc^2)	(10^2pc)
0	trunk	6.01	46.27	2.21	26.11 x 77.83	71.13	32.00	23.37	14.63
1	leaf	2.57	6.60	0.22	14.08 x 16.43	17.35	4.44	1.82	2.54
2	trunk	6.01	39.94	1.73	19.74 x 75.56	60.26	21.49	19.96	12.66
3	leaf	1.96	9.01	0.46	5.8 x 7.75	nan	0.74	0.46	1.08
4	leaf	3.77	19.62	0.83	19.96 x 15.67	22.72	7.84	5.97	5.02
5	trunk	6.01	36.84	1.72	18.56 x 75.73	58.34	16.17	14.34	11.59
6	leaf	1.67	12.20	0.56	21.8 x 6.03	6.10	16.27	1.50	2.57
7	leaf	2.49	22.61	1.04	15.61 x 25.64	27.33	10.60	3.36	3.85
8	trunk	6.01	33.48	1.55	18.4 x 75.78	58.09	14.25	13.81	10.99

NOTE—Table of observed properties of the ^{13}CO(2-1) emission of the Antennae overlap where "ncl" is the cloud number, "clump type" is the dendrogram structure type of the cloud, "CO max" is the maximum brightness in the clump, "σ_v" is the velocity dispersion, "maj x min" are the major and minor axes of the clump, and "R" is the clump's effective radius. The first 10 structures are shown here with the full table being available upon request

REFERENCES

Ashman, K. M., & Zepf, S. E. 2001, AJ, 122, 1888, doi: 10.1086/323133

Astropy Collaboration, Robitaille, T. P., Tollerud, E. J., et al. 2013, A&A, 558, A33, doi: 10.1051/0004-6361/201322068

Astropy Collaboration, Price-Whelan, A. M., Sipőcz, B. M., et al. 2018, AJ, 156, 123, doi: 10.3847/1538-3881/aabc4f

Bigiel, F., Leroy, A. K., Blitz, L., et al. 2015, ApJ, 815, 103, doi: 10.1088/0004-637X/815/2/103

Blake, G. A., Sutton, E. C., Masson, C. R., & Phillips, T. G. 1987, ApJ, 315, 621, doi: 10.1086/165165

Elmegreen, B. G. 1989, ApJ, 338, 178, doi: 10.1086/167192

Elmegreen, B. G., & Efremov, Y. N. 1997, ApJ, 480, 235, doi: 10.1086/303966

Falgarone, E., Phillips, T. G., & Walker, C. K. 1991, ApJ, 378, 186, doi: 10.1086/170419

Finn, M. K., Johnson, K. E., Brogan, C. L., et al. 2019, ApJ, 874, 120, doi: 10.3847/1538-4357/ab0d1e

Finn, M. K., Indebetouw, R., Johnson, K. E., et al. 2021, ApJ, 917, 106, doi: 10.3847/1538-4357/ac090c

Gilbert, A. M., & Graham, J. R. 2007, ApJ, 668, 168, doi: 10.1086/520910

Harris, C. R., Millman, K. J., van der Walt, S. J., et al. 2020, Nature, 585, 357, doi: 10.1038/s41586-020-2649-2

Harris, W. E., & Pudritz, R. E. 1994, ApJ, 429, 177, doi: 10.1086/174310

Heyer, M., Krawczyk, C., Duval, J., & Jackson, J. 2008, Astrophysical Journal - ASTROPHYS J, 699, doi: 10.1088/0004-637X/699/2/1092

Hsieh, P.-Y., Matsushita, S., Liu, G., et al. 2011, The Astrophysical Journal, 736, 129, doi: 10.1088/0004-637x/736/2/129

Imara, N., & Faesi, C. M. 2019, ApJ, 876, 141, doi: 10.3847/1538-4357/ab16cc

Johnson, K. E., Leroy, A. K., Indebetouw, R., et al. 2015, ApJ, 806, 35, doi: 10.1088/0004-637X/806/1/35

Larsen, S. S. 2010, Philosophical Transactions of the Royal Society of London Series A, 368, 867, doi: 10.1098/rsta.2009.0255

Larson, R. B. 1981, MNRAS, 194, 809, doi: 10.1093/mnras/194.4.809

Leroy, A., Bolatto, A., Walter, F., & Blitz, L. 2006, ApJ, 643, 825, doi: 10.1086/503024

Leroy, A. K., Bolatto, A. D., Ostriker, E. C., et al. 2015, ApJ, 801, 25, doi: 10.1088/0004-637X/801/1/25

Mangum, J. G., & Shirley, Y. L. 2015, PASP, 127, 266, doi: 10.1086/680323

McCrady, N., & Graham, J. R. 2007, ApJ, 663, 844, doi: 10.1086/518357

McLaughlin, D. E., & Fall, S. M. 2008, ApJ, 679, 1272, doi: 10.1086/533485

Miura, R. E., Espada, D., Hirota, A., et al. 2018, The Astrophysical Journal, 864, 120, doi: 10.3847/1538-4357/aad69f

Miyazaki, A., & Tsuboi, M. 2000, ApJ, 536, 357, doi: 10.1086/308899

O'Connell, R. W., Gallagher, John S., I., & Hunter, D. A. 1994, ApJ, 433, 65, doi: 10.1086/174625

Oka, T., Hasegawa, T., Sato, F., et al. 2001, ApJ, 562, 348, doi: 10.1086/322976

Rosolowsky, E. 2007, ApJ, 654, 240, doi: 10.1086/509249

Rosolowsky, E., Keto, E., Matsushita, S., & Willner, S. P. 2007, The Astrophysical Journal, 661, 830, doi: 10.1086/516621

Rosolowsky, E., Hughes, A., Leroy, A. K., et al. 2021, Monthly Notices of the Royal Astronomical Society, 502, 1218, doi: 10.1093/mnras/stab085

Rosolowsky, E. W., Pineda, J. E., Kauffmann, J., & Goodman, A. A. 2008, The Astrophysical Journal, 679, 1338, doi: 10.1086/587685

Sánchez, N., Alfaro, E. J., & Pérez, E. 2007, ApJ, 656, 222, doi: 10.1086/510351

Schweizer, F., Burns, C. R., Madore, B. F., et al. 2008, AJ, 136, 1482, doi: 10.1088/0004-6256/136/4/1482

Sidorin, V. 2017, Quickclump: Identify clumps within a 3D FITS datacube, Astrophysics Source Code Library, record ascl:1704.006. http://ascl.net/1704.006

Solomon, P. M., Rivolo, A. R., Barrett, J., & Yahil, A. 1987, ApJ, 319, 730, doi: 10.1086/165493

Tosaki, T., Kohno, K., Harada, N., et al. 2017, Publications of the Astronomical Society of Japan, 69, doi: 10.1093/pasj/psw122

Tsuge, K., Fukui, Y., Tachihara, K., et al. 2021, PASJ, 73, S35, doi: 10.1093/pasj/psaa033

Utomo, D., Blitz, L., Davis, T., et al. 2015, ApJ, 803, 16, doi: 10.1088/0004-637X/803/1/16

van den Bergh, S., Morbey, C., & Pazder, J. 1991, ApJ, 375, 594, doi: 10.1086/170220

Virtanen, P., Gommers, R., Oliphant, T. E., et al. 2020, Nature Methods, 17, 261, doi: 10.1038/s41592-019-0686-2

Wei, L. H., Keto, E., & Ho, L. C. 2012, ApJ, 750, 136, doi: 10.1088/0004-637X/750/2/136

Whitmore, B. C., Brogan, C., Chandar, R., et al. 2014, ApJ, 795, 156, doi: 10.1088/0004-637X/795/2/156

Wong, T., Hughes, A., Ott, J., et al. 2011, ApJS, 197, 16, doi: 10.1088/0067-0049/197/2/16